2026 IEEE International Conference on Robotics and Automation (ICRA 2026)
June 1-5, 2026. Vienna, Austria

Development of Remote Center of Motion Mechanism for Biportal Endoscopic Spine Surgery Robot

Chunwoo Kim[1,2], Chaewon Kim[1,3], and Dongeun Choi[1,4]

***Abstract*— Remote Center of Motion (RCM) mechanism is widely used in surgical robots for Minimally Invasive Surgery (MIS). For endoscopic spine surgery, the surgical robot requires RCM mechanism with sufficient stiffness and compact end effector to manipulate hard tissues while avoiding interference with other instruments. This paper presents a modified belt-driven RCM mechanism designed to meet these specific requirements of the endoscopic spine surgery. Gearboxes were incorporated to the belt-driven Remote Center of Motion (RCM) mechanism to reduce belt tension and resulting elastic deformation, while the RCM constraint is maintained through a specific relationship between gearbox reduction ratios. The prismatic joint for instrument insertion is relocated to the base to reduce the size of the end effector. Prototype of a surgical robot with the presented RCM mechanism achieved an RCM point accuracy of 0.56 mm, repeatability of 0.019 mm, and stiffness of 11.676, 12.435, and 5.341 N/mm in the X, Y, and Z directions, respectively. Feasibility of the robot was validated through simulated BESS on a spine phantom.**

I. INTRODUCTION

In minimally invasive surgery (MIS), the motion of surgical instruments is characterized by a 4 degrees of freedom (DoF) motion constrained at the minimal incision point on the patient's body. These 4 DoFs consist of two rotational DoFs around the incision, one translational DoF for inserting the instrument through the incision, and one rotational DoF around the instrument shaft. Surgical robots for MIS must implement such constrained motion either through mechanism [1] or via robot motion control [2]. Consequently, the Remote Center of Motion (RCM) mechanism, a mechanism that generates constrained rotational motion around a fulcrum point (RCM point) located outside the mechanism's body, has been widely adopted in surgical robots [1]. Various types of RCM mechanisms - including double parallelogram [3], [4], [5], belt or cable driven [6], [7], [8], spherical linkage [9], and circular guide [10], [11] - have been designed and applied to surgical robots across various specialties such as laparoscopic surgery [12], eye surgery [13], interventional radiology [14] and bone surgery [11], [15].

Biportal Endoscopic Spine Surgery (BESS) is a minimally invasive surgical procedure used to treat spinal stenosis [16]. During BESS, surgeon makes two small incisions on the patient's back. Then, an arthroscope is inserted through one incision, while surgical instruments such as punches and burrs are inserted through the other, as shown in Fig. 1a. The surgeon manipulates the arthroscope and the instruments to remove bones, ligaments and herniated disc to decompress the spinal cord.

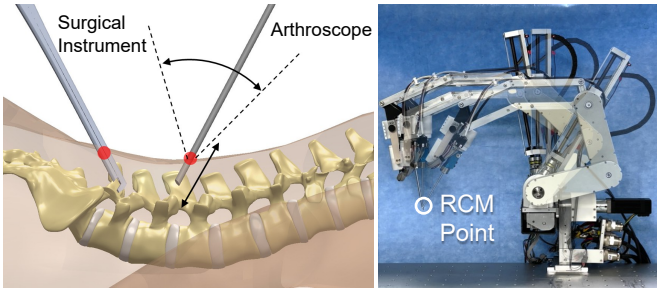

Fig. 1. a) Illustration of Biportal Endoscopic Spine Surgery (BESS) and motion of the instruments. b) RCM mechanism of the BESS robot implementing the instrument motion.

Thus, a surgical robot for BESS should have a RCM mechanism to manipulate the instruments inserted through small incisions, similar to robots for laparoscopic surgery. However, unlike laparoscopic surgery robots, which primarily interact with soft tissues, a BESS robot must manipulate stiff tissues such as tendons and bones, resulting in higher contact forces. Therefore, the robot must possess sufficient stiffness to withstand these forces without significant deformation.

Also, during BESS, an X-ray fluoroscope is positioned over patient to provide intraoperative imaging. Therefore, the robot's end effector must be compact enough to avoid interference with the overhanging fluoroscope, as well as other instruments sharing the surgical field.

To date, most robots developed for spine surgery have been shared-control systems designed to assist with pedicle screw placement during spinal fusion [17], [18], [19]. Only a few studies have investigated the use of the teleoperated da Vinci robot—originally developed for laparoscopic surgery—in anterior lumbar interbody fusion (ALIF) or arthroscopic procedures [20], [21]. However, teleoperated surgical robots specifically dedicated to endoscopic spine surgery or other arthroscopic procedures have not yet been commercialized [22], [23].

As a first step towards a teleoperated surgical robot tailored for spine surgery, this paper presents the development of an RCM mechanism of a teleoperated surgical robot for BESS.

*This work was supported by the Technology Innovation Program (20009071) funded by the Ministry of Trade, Industry and Energy (MOTIE), Korea, and Institutional Program (26E0171) of Korea Institute of Science and Technology

[1] Korea Institute of Science and Technology, Seoul, Korea.
[2] University of Science and Technology, Daejon, Korea.
[3] Korea University, Seoul, Korea.
[4] Asan Medical Center, Seoul, Korea.
Corresponding Author : Chunwoo Kim (cwkim@kist.re.kr)

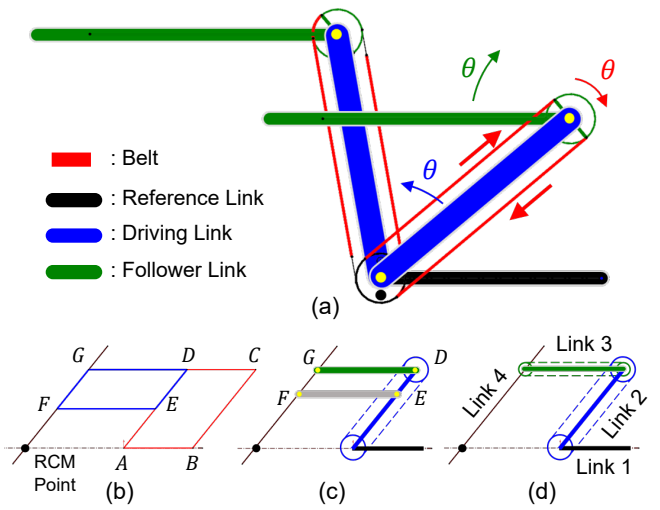

Fig. 2. a) Principle of the belt parallelogram. b) Double parallelogram RCM mechanism. c,d) Belt-driven RCM mechanism formed by replacing the 4 bar parallelogram *ABCD* and *EFGD* with the belt parallelogram formed by link 1-2-3 and link 2-3-4, respectively

To meet the aforementioned requirements of the robot — sufficient stiffness and a compact end effector — two design modifications were made to a belt-driven RCM mechanism commonly used in surgical robots. The details of these design modifications and the evaluation of the robot incorporating the developed RCM mechanism are provided in the following sections.

II. Design

Among the various types of the RCM mechanisms, the belt-driven RCM mechanism offers several advantages over other types, including a reduced number of links and joints, smaller size, unrestricted rotations about the RCM point, and elimination of singular points [6]. As a result, it is one of the most commonly employed RCM mechanism in surgical robots for MIS, as exemplified by its use in several commercial laparoscopic surgery robots such as daVinci (Intuitive Surgical, USA), Revo-i (Meere Company, Korea) and Hugo (Medtronic, USA).

Fig. 2 shows the structure and principles of the typical belt-driven RCM mechanism. The core component of the mechanism is the belt parallelogram shown in Fig. 2a. The belt parallelogram consists of three links, reference, driving and follower links, serially connected by two revolute joints. Pulleys are installed at each joint, fixed to the reference and the follower links, respectively. The belt connecting the two pulleys couples the rotation of the driving link and the follower link, constraining the orientation of the follower link such that it remains constant with respect to the reference link throughout the rotation of the driving link.

The belt-driven RCM mechanism is constructed by replacing one or both four-bar parallelogram of the double parallelogram RCM mechanism with 'belt parallelograms', as shown in Fig. 2b-d. The mechanism generates two rotational motions of the output link (link $\overline{GF}$) about the RCM

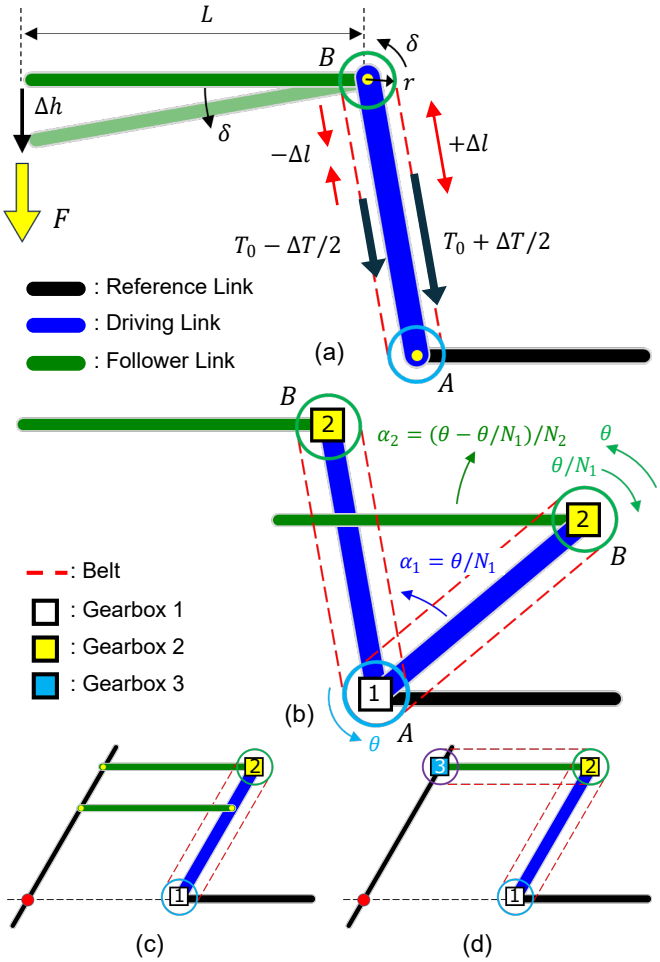

Fig. 3. a) Static analysis of belt parallelogram b) Modifications to the belt parallelogram to increase the stiffness. Input-output of the gearbox 1 and 2 are pulley *A*-driving link and pulley *B*-output link, respectively. c,d) RCM mechanism using c) one and d) two modified belt parallelograms.

point. For the BESS robot, this belt-driven RCM mechanism is modified to enhance stiffness and reduce the size of the end effector at the output link, as explained in the following section.

A. Design modifications 1 : Enhancing Stiffness

Fig. 3a shows the static analysis of the belt parallelogram used in current belt-driven RCM mechanisms. When load F is applied to the end of the follower link of length L, joint torque $\tau = FL$ is directly transmitted to the pulley B with radius r. This joint torque is balanced by the difference of the belt tension

$$\Delta T = \frac{FL}{r} \tag{1}$$

across the pulley B, generated by the increase of the tension by $\Delta T/2$ on one side of the belt and the decrease of the tension by the same amount on the other side. As a result, the belt with spring constant k stretches on one side by $\Delta l = \frac{\Delta T}{2k}$ and shrinks by same amount $-\Delta l$ on the other. This deformation of the belt allows the pulley B and the follower link connected to it to rotate freely by angle

$$\delta = \frac{2\Delta l}{r} = \frac{\Delta T}{kr} = \frac{\tau}{kr^2} \tag{2}$$

and result displacement

$$\Delta h = L\delta = \frac{L\Delta T}{kr} = \frac{FL^2}{kr^2} \tag{3}$$

at the end of the follower link.

This analysis shows that in current belt-driven RCM mechanisms, the external forces and torques applied to the follower link are directly transferred to and balanced by the tension of the belt, and the deformation of theses belts under tension leads to the displacement. It also shows that the stiffness of the mechanism can be increased by using larger pulley, or by increasing the stiffness of the belt, which will increase the size of the mechanism or require use of special metal belts as in [12]. The stiffness of the belt-driven RCM mechanism is fundamentally limited by the stiffness of the belt. As a result, the use of belt-driven RCM mechanisms has been limited to the surgical robots for laparoscopic surgery manipulating soft tissues, and alternative RCM mechanisms have been chosen for applications requiring higher stiffness for manipulating hard tissues [11], [15].

In the modified belt-driven RCM mechanism presented in this paper, instead of directly connecting the pulleys to the links, the gearboxes are installed between the pulleys and the links to reduce the joint torques and tensions transmitted to the belts and resulting deformations. Fig. 3b shows the structure of the belt parallelogram of the modified RCM mechanism. Pulleys A and B are connected to the driving link and the follower link through the gearbox 1 and 2 with reduction ratio N_1 and N_2, respectively, and two pulleys are connected by a belt. When the joint torque $\tau = FL$ applied to the follower link, the gearbox 2 reduces it by $1/N_2$ and transmits it to the pulley B. Thus the tension difference across the belt and the resulting displacement of the follower link is also reduced by the same amount,

$$\Delta T = \frac{FL}{N_2 r} \tag{4}$$

$$\Delta h = \frac{L\Delta T}{kr} = \frac{FL^2}{N_2 kr^2} \tag{5}$$

which leads to the increased stiffness of the belt parallelogram by N_2.

However, in this modified belt parallelogram, special relationship between the reduction ratios of the gearboxes must be satisfied in order to ensure that the orientation of the follower link remains constant throughout the rotation of the driving link. As shown in Fig. 3b, when pulley A is rotated by θ, driving link will rotate by

$$\alpha_1 = \theta/N_1 \tag{6}$$

This rotation of the driving link respect to the pulley A by α_1 generates the rotation of the belt and pulley B by $-\alpha_1 = -\theta/N_1$. simultaneously, the rotation of pulley A is transmitted to the pulley B through the belt and rotates the pulley B by θ. Thus, the net rotation of the pulley B is $\theta - \theta/N_1$, which is reduced by N_2 and rotates the follower link by

$$\alpha_2 = (\theta - \theta/N_1)/N_2 \tag{7}$$

If the reduction ratio of the gearboxes are selected such that

$$N_2 = -(N_1 - 1) \tag{8}$$

then $\alpha_1 = -\alpha_2$ and the orientation of the follower link remains unchanged.

This modified belt parallelogram with increased stiffness can be combined with a double parallelogram or another modified belt parallelogram to form a RCM mechanism as shown in Fig. 3c and d. When combining two belt parallelograms as illustrated in Fig. 3d, the reduction ratios of the two gearboxes of the second belt parallelogram, gearbox 2 and 3, must also satisfy (8). Thus, the reduction ratio N_3 of the third gearbox would be

$$N_3 = -(N_2 - 1) = -(-(N_1 - 1) - 1) = N_1 \tag{9}$$

The relationship between the reduction ratios of the gearboxes specified in (8) can be easily achieved using two identical harmonic drives with a reduction ratio R, arranged in different input and output configuration. For both gearboxes 1 and 2, pulley is connected to the wave generator of the harmonic drive. In gearbox 1, the circular spline of the harmonic drive is fixed and the driving link is connected to the flexible spline of the harmonic drive. Then, the input rotation of the pulley is transmitted to the output rotation of the driving link, reduced by $N_1 = -R$. In gearbox 2, the flexible spline fixed and the follower link is connected to the circular spline. In this configuration, the input rotation of the pulley is transmitted to the output rotation of the follower link, reduced by $N_2 = (R+1) = -(N_1 - 1)$, satisfying the constraints in (8).

B. Design modifications 2 : Compact end effector

In surgical robots for MIS, a prismatic joint that provides an additional DoF for instrument insertion is typically installed at the output link of the RCM mechanism, as shown in Fig. 4a. The linear guide and actuators of the prismatic joint increase the size and inertia of the robot's end effector. In BESS, such large end effector with a prismatic joint may limit the robot's motion and hinder the use of intraoperative X-ray imaging, as observed in previous research using the daVinci robot for similar arthroscopic surgery [21].

In the modified belt-driven RCM mechanism presented in this paper, the prismatic joint for instrument insertion is moved from the output link to the driving link $\overline{AB}$ of the belt parallelogram, as shown in Fig. 4b, to reduce the size of the end effector and avoid the interference. As a result, the length of the driving link varies with the motion of the prismatic joint. Then, to maintain belt connection between the pulleys at both ends A and B of the driving link despite the link length change, belts are routed through scissor links $\overline{AC}$ and $\overline{CB}$ that connects the both ends.

The idea of using prismatic joint and scissor links to add translational DoF in RCM mechanism has been reported in

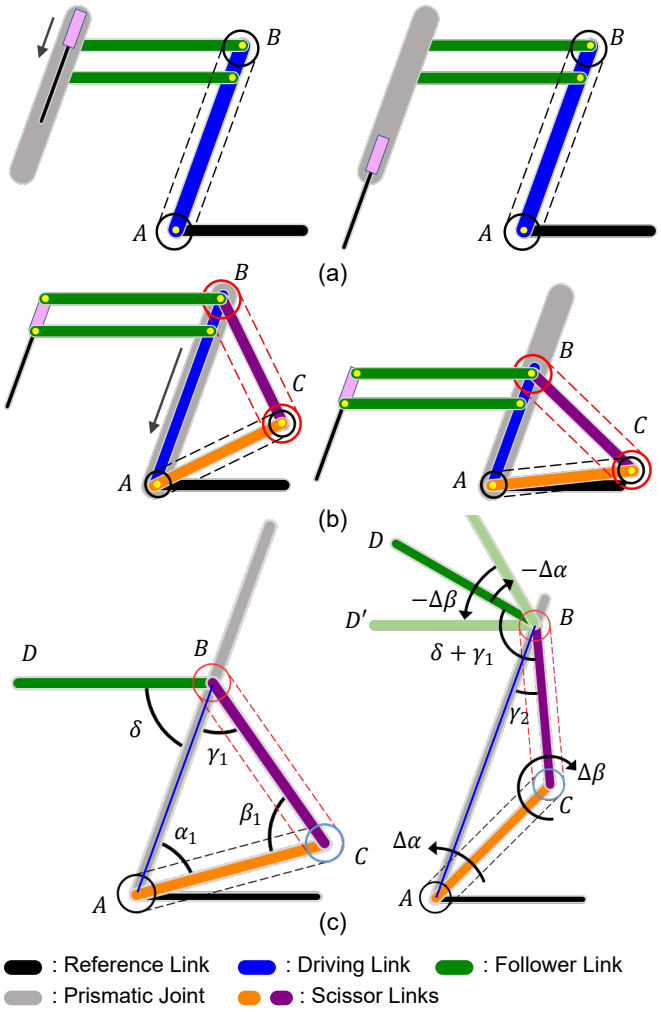

Fig. 4. a) Typical placement of a prismatic joint at the output link of the RCM mechanism b) Moving prismatic joints to the driving link c) Analysis of belt rotation during the motion of the prismatic joint

previous literature [13], [24], [4], [5] for double parallelogram RCM mechanisms. However, to apply this idea to the belt-driven RCM mechanism, it must be assured that the orientation of the follower link remains constant during the motion of the prismatic joint, as shown in Fig. 4c. When the prismatic joint moves, the lower scissor link $\overline{AC}$ rotates by $\Delta\alpha$ relative to the pulley A, the upper scissor link $\overline{CB}$ rotates by $\Delta\beta$ relative to the the pulley C, and these rotations are transferred by the belt to rotate the pulley B and the output link connected to it $\overline{BD}$ by $-\Delta\alpha-\Delta\beta$. Since $\alpha_1+\beta_1+\gamma_1=180°$, $\Delta\gamma=-\Delta\alpha-\Delta\beta$. Thus $\angle D'BC=\angle DBC+\Delta\gamma=\delta+\gamma_1+\Delta\gamma=\delta+\gamma_2$, and $\angle D'BA=\angle D'BC-\gamma_2=\delta=\angle DBA$, which indicates that the orientation of the follower link remains constant with respect to the reference link during the translational motion by prismatic joint.

III. Implementation and Evaluation

The modified belt-driven RCM mechanism described in the previous section is applied to the Minimally Invasive Spine Surgery (MISS) robot, a teleoperated surgical robot

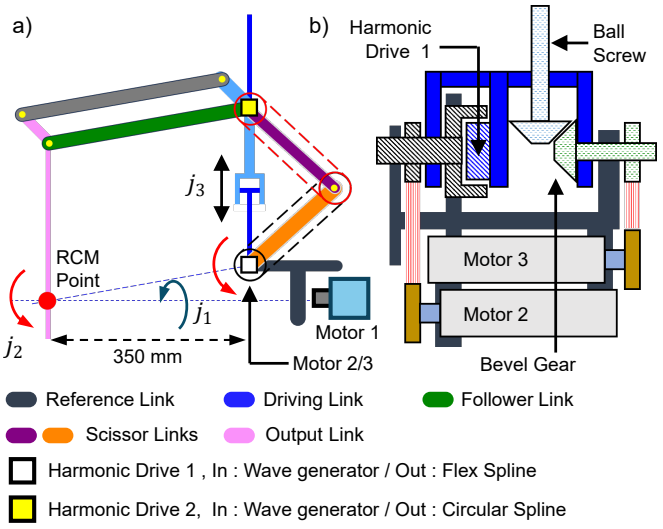

Fig. 5. a) Kinematic structure of the RCM mechanism in the MISS Robot. b) Placement of Motor 2/3 and motion transmission on the reference link

for BESS. The following sections explain the structure of the robot and the evaluation of its RCM motion and stiffness.

A. Kinematic Structure of MISS Robot

The kinematic structure of the RCM mechanism of the MISS Robot is shown in Fig. 5a. The RCM point is located 350 mm away from the base of the robot. The robot has 3 DoFs. Joint 1 is driven by the motor 1 that rotates the entire mechanism about the axis passing the RCM point. Joint 2 rotates the driving link through the gearboxes, which leads to the rotation of the output link about the RCM point through the parallelogram mechanisms. Harmonic drives with reduction ratio 100 were used as the gearboxes to increase the stiffness of the robot as discussed in the previous section, resulting reduction ratios of -100 and 101 for gearbox 1 and 2 respectively. The pulleys at the inputs of two harmonic drives are connected with rubber timing belts. Since the harmonic drives reduce the tensions transmitted to the belts from the external loads, the robot can benefit from the precision of the timing belt transmission without compromising its overall stiffness. The prismatic joint 3 is installed at the driving link of the mechanism, as discussed in the previous section. To provide high stiffness in tool insertion degrees of freedom as well, the prismatic joint is implemented using ball screw mechanism for its high mechanical advantage.

Fig. 5b shows the placement of the motor 2 and 3 driving the joint 2 and 3, respectively. To reduce the inertia of the driving link, motor 3 is installed on the reference link instead of the driving link, and is connected to the ball screw through a bevel gearbox. This setup allows the stationary motor 3 to transmit motion to the ball screw on the driving link, which rotates relative to the reference link.

The actual prototype of the MISS robot is shown in Fig. 1b. Handpiece with the burr blade is installed as an end effector of the robot. The range of motion for each joint is $(-45,45)°$, $(-10,45)°$, and $(+110,-110)mm$ for joint 1,2 and 3, respectively, reflecting the surgical instrument

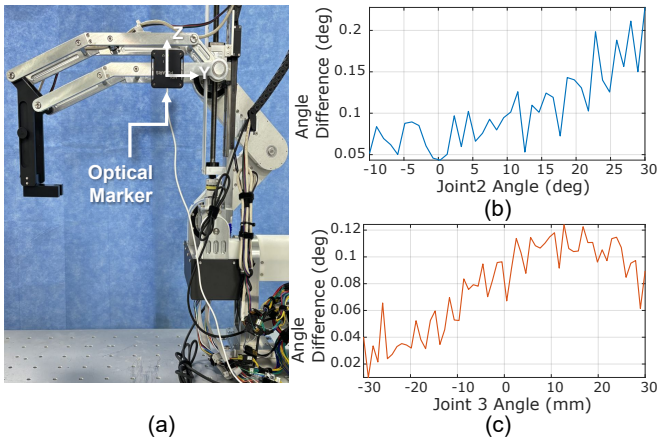

Fig. 6. a) Experiment setup for measuring the orientation of the follower link. b, c) Variation of the marker coordinate system orientation during the motion of b) joint 2 and c) joint 3.

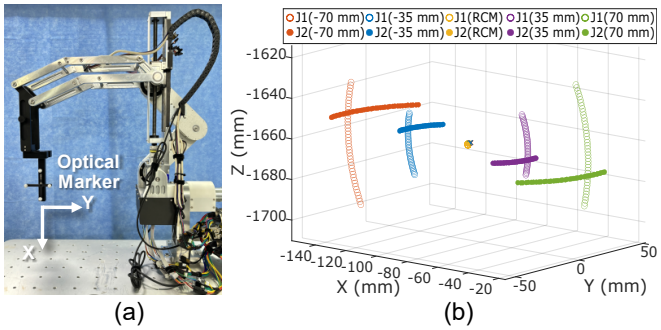

Fig. 7. a) Experiment setup for RCM point accuracy measurement 2 b) Trajectory of the marker and the location of the RCM point

movement range in BESS. The supplementary video shows the motion of the robot's 3 DoFs at orients and inserts the burr blade about the RCM point.

B. Evaluation of the RCM Motion

Three experiments were conducted to evaluate the RCM motion of the robot. In the experiments, the robot was moved in various positions within its joint workspace and the robot's motion was recorded using an optical tracker (NDI Polaris, Northern Digital) with 0.3 mm rms accuracy.

In the first experiment, the orientation of the follower link was measured to confirm that the constraints of the belt-driven RCM mechanism, - which ensures that the orientation of the follower link with respect to the reference link remain constant throughout the robot's motion - is preserved despite the modifications to the mechanism introduced in this research. Optical marker was attached to the follower link as shown in Fig. 6a and the rotation matrix R that represents the orientation of the marker coordinate system with respect to the tracker coordinate system was recorded as:

1) Joint 2 moved from -10° to 30° in steps of 1° and
2) Joint 3 moved from -30 to 30 mm in steps of 1 mm

From the measurement data, the variation of the orientation was evaluated by calculating the rotation angle $\Delta\theta$ between the measured rotation matrix R and its initial value R_0 using the equation

$$\Delta\theta = \arccos\left(\frac{tr(R_0^T R) - 1}{2}\right) \tag{10}$$

Fig. 6b and c shows the variation of the follower link's orientation during the motion of the joint 2 and 3, respectively. The orientation of the marker coordinate system deviated by up to 0.22° from the initial configuration during the motion of joint 2, and up to 0.12° during the motion of joint 3. These results show that the orientation of the follower link remains nearly unchanged during both rotational and translational motions, confirming that the constraints of the mechanism is preserved.

In the second experiment, accuracy of the RCM motion was evaluated by measuring the location of the RCM point from the trajectory of the robot's end effector. An optical marker was attached as the robot's end effector in place of a surgical instrument. The marker was attached such that the origin of the marker coordinate system coincide with the RCM point when the robot is at its zero configuration, as shown in Fig. 7a. Then, joint 3 was moved to translate the origin to 5 different instrument insertion depths : 0 mm (RCM point) and $\pm$35 mm, $\pm$70 mm away from the RCM point. At each depth, the position of the marker coordinate system origin was recorded as:

1) Joint 1 was moved from -10° to 30° in steps of 1° while joint 2 was fixed at 0° and
2) Joint 2 was moved from -10° to 30° in steps of 1° while joint 1 was fixed at 0°.

Pivot calibration [25] was performed on the positions measured at each depth to identify the location of the pivot point of the motion, which corresponds to the RCM point. Also, the distance between the identified RCM point and the points on the trajectory was calculated.

The measured positions of the marker coordinate system origin and the location of the RCM point identified from the pivot calibration is plotted in Fig. 7b. The figure shows the circular trajectory about consistent center point for all 5 different insertion depths, indicating accurate RCM motion. Quantified result is summarized in Table I. The mean value of the distance between the points on the trajectory and the identified RCM point differs slightly from the insertion depth. This indicates that the origin of the marker coordinate system was slightly offset from the RCM point when the robot was in zero configuration, possibly due to the small

TABLE I
RCM ACCURACY MEASUREMENT

Insertion depths(mm)	RCM Point Position X(mm)	Y(mm)	Z(mm)	Mean distance from the RCM point (mm)
+35	-84.997	-2.55	-1661.5	35.40 ± 0.083
+70	-84.945	-2.29	-1661.5	70.29 ± 0.080
0	-84.992	-3.01	-1661.6	1.08 ± 0.084
-35	-84.942	-3.38	-1661.6	34.19 ± 0.093
-70	-85.064	-3.36	-1661.5	69.31 ± 0.106
Stdev	0.049	0.557	0.049	

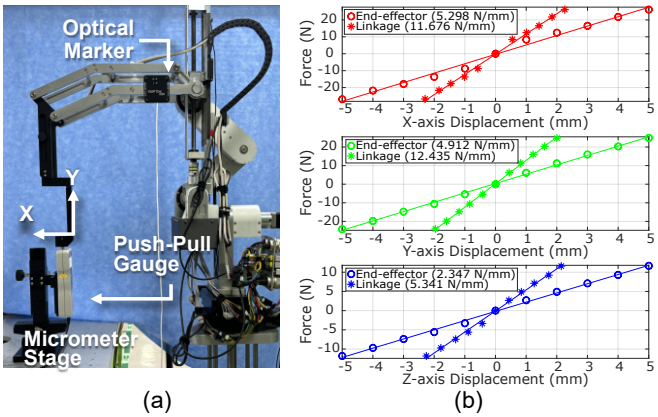

Fig. 8. a) Experiment setup for measuring the stiffness. b) Measured force displacement curve in X, Y, Z direction

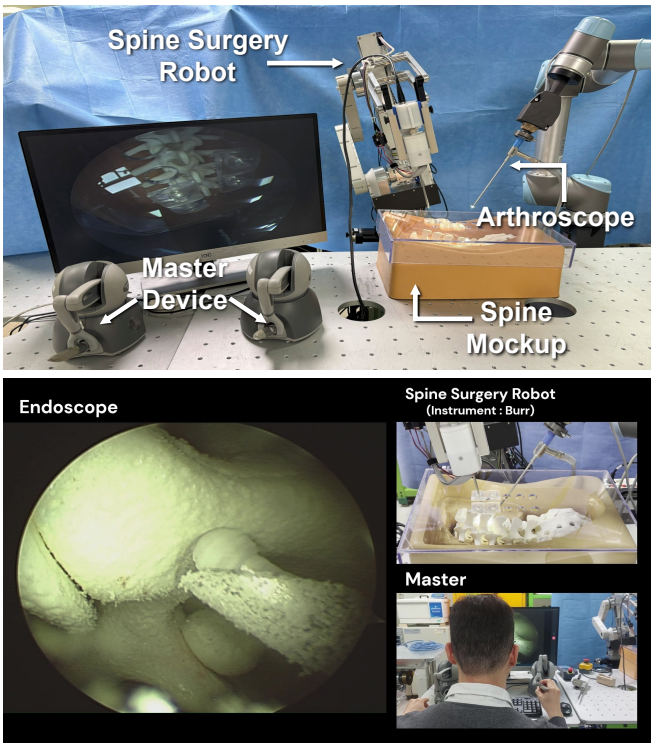

Fig. 9. (Top) Teleoperated system for spine surgery on a mockup using a master device, surgical robot and arthroscope. (Bottom) View of the arthroscope and robot during simulated surgery.

error during the assembly of the marker or homing of the robot joints. However, the standard deviation of the distances were within 0.1 mm for all 5 depths, which means that the motion generated by both joint 1 and 2 are very close to pure rotation motion about the RCM point. Furthermore, the position of the RCM point identified from the pivot calibration were almost identical for all 5 depths, with standard deviations of 0.049, 0.557 and 0.049 mm in X, Y and Z coordinate and 0.56 mm overall, indicating that the position of the RCM point remains constant throughout the motion of the robot.

Lastly, in the third experiment, the repeatability of the robot was evaluated by moving the robot to different positions in joint coordinates. The robot was initially positioned to the zero configuration $P0 = (0°, 0°, 0mm)$. Then, from $P0$, the robot was moved to $P1 = (-10°, -10°, -70mm)$, then to $P2 = (30°, 30°, 70mm)$ and then back to $P0$. This entire sequence was repeated 20 times, while the optical tracker recorded the position of the marker when the robot returned to the $P0$. The the standard deviation of the 20 measurements at $P0$ were 0.017, 0.013, 0.025 mm in the X, Y and Z axes and 0.019 mm overall, indicating a high level of repeatability of the robot.

C. Stiffness

Fig. 8a shows the setup for measuring the stiffness of the robot. The setup was designed to simulate an surgical instrument in contact with the stiff tissue during BESS. An end effector simulating the surgical instrument was assembled to the robot. Tip of the end effector was positioned 35 mm below the RCM point along the instrument axis, considering the insertion depth of the instrument during BESS. Push pull gauge (DSV-200, IMADA) mounted on an XYZ micrometer stage was connected to the end effector tip. Force was applied to the robot in a controlled manner by translating the stage in 1 mm increments along the $\pm X$, $\pm Y$ and $\pm Z$ directions. Displacement of the end effector tip and the corresponding force was measured. At the same time, to measure the stiffness of the robot excluding that of the end effector, an optical marker was attached to the follower link of the robot, and the displacement of the link was measured.

Fig. 8b shows the resulting force-displacement curve obtained from the experiment. Stiffness was calculated as the slope of the force-displacement curve fitted to the measured data using least squares method. The stiffness at the end effector tip were determined to be 5.298, 4.912 and 2.347 N/mm, in the X, Y and Z axes, respectively. The stiffness at the follower link was determined to be 11.676, 12.435 and 5.341 N/mm in the X, Y and Z axes, respectively.

The stiffness at the follower link were larger than the stiffness at the end effector, and also are more direct evaluation of the robot mechanism's stiffness because it does not include the deformation of the end effector itself. The stiffness of the robot mechanism in X and Y direction is pertains to the stiffness of the belt parallelogram, as analyzed in Fig. 3a. This explains smallest stiffness in Z axis as it is not affected by the increased stiffness of the belt parallelogram.

Previous researches measuring force during bone burring reported forces up to 6.1 N [26], [27]. The measured stiffness values indicate that the maximum deflection of the robot mechanism will be less than 1 mm in X and Y direction during bone burring. These results suggest that the robot can effectively withstand the force encountered in BESS.

D. Simulated Surgery

Finally, the feasibility of the robot was tested in the simulated surgery on the mockup (Spine Holder Set, Sawbones). Handpiece with burr blade was installed as the end effector of the robot. The robot was teleoperated using Phantom

Omni master device while the mockup was viewed from a arthroscope held by a commercial robot arm, as shown in Fig. 9. The supplementary video shows the successful burring of the spine mockup with the teleoperated robot.

IV. Discussion

This paper presents a modified design of the belt-driven RCM mechanism that satisfies the requirements of a surgical robot for BESS. The design modification were made to improve the stiffness of the robot for manipulating stiff tissues and reduce the size of the end effector to avoid interference with other medical devices during the surgery.

Surgical robot with the modified RCM mechanism was evaluated through series of experiments and mockup surgery. The experiment result shows that the modifications preserved the constraints of the RCM mechanism and the robot functions as an RCM mechanism with stable RCM point capable of generating 2 DoF rotation motion about RCM point plus an additional translational DoF for instrument insertion with high repeatability. The modification improved the stiffness of the mechanism to ensure that the deflection of the mechanism is less than 1 mm in X and Y directions under the reported contact force during bone burring. While the stiffness improvement using gearbox comes with the price of the decreased dynamic performance, the performance of the robot was successfully validated in mockup surgery.

Among the previous researches on the RCM mechanisms, two researches, [10], [11] and [4], [8], present ideas similar to those explored in this research. Shim et. al. [10], [11] developed RCM mechanism with emphasis on the high stiffness for bone drilling applications. The mechanism achieved high stiffness by using circular guides to provide RCM motion constraint and lead screw to provide stiff actuation. However, since the end effector travels along the circular guide, the guide must be positioned above the RCM point, and the range of the RCM motion is limited by the central angle of the circular guide. In contrast, the belt-driven RCM mechanism allows for a larger motion range and reduces obstruction above the RCM point.

Long et. al [4], [8] proposed an RCM mechanism that implements both rotational and translational motion. In particular, [8] introduced a steel cable-driven serial link that achieves combined rotational and translational RCM motion without prismatic joints by imposing specific constraints on the pulley radius. In the presented RCM mechanism, instead of steel cables, polymer timing belts and gearboxes were employed to improve accuracy while decreasing the elastic deformation of the belts. At the same time, RCM constraints was preserved through a specific ratio between the reduction ratios of the gearboxes. This led to an RCM point accuracy of 0.56 mm and repeatability of 0.019 mm.

Overall, the presented RCM mechanism retains the advantages of the belt-driven RCM mechanism widely used in the minimally invasive surgical robot, while adapting its design to meet the requirements of the BESS. The mechanism holds potential for broader application to other arthroscopic procedures, which share similar characteristics with BESS, including the minimally invasive manipulation of stiff tissues and the need to operate in environments constrained by large overhead X-ray equipment.

For the future works, the structural stiffness of the output link and the end effector will be improved to match the stiffness in Z direction to that of the RCM mechanism. Additional surgical instruments for BESS - including Kerrison punch and Pituitary Rongeur - will be developed for robot's end effector, along with corresponding instrument exchange mechanisms. Also, the robot will be integrated with a better vision system and teleoperation leader device. Finally, comprehensive evaluations of the robot's performance will be conducted in cadaveric environments.

References

[1] C. H. Kuo, J. S. Dai, and P. Dasgupta, "Kinematic design considerations for minimally invasive surgical robots: an overview," *International Journal of Medical Robotics and Computer Assisted Surgery*, vol. 8, no. 2, pp. 127–145, 2012.

[2] N. Aghakhani, M. Geravand, N. Shahriari, M. Vendittelli, and G. Oriolo, "Task control with remote center of motion constraint for minimally invasive robotic surgery," *2013 Ieee International Conference on Robotics and Automation (ICRA)*, pp. 5807–5812, 2013.

[3] R. H. Taylor, J. Funda, B. Eldridge, S. Gomory, K. Gruben, D. Larose, M. Talamini, L. Kavoussi, and J. Anderson, "A telerobotic assistant for laparoscopic surgery," *Ieee Engineering in Medicine and Biology Magazine*, vol. 14, no. 3, pp. 279–288, 1995.

[4] L. Huang, Y. Yang, J. J. Xiao, and P. Su, "Type synthesis of 1r1t remote center of motion mechanisms based on pantograph mechanisms," *Journal of Mechanical Design*, vol. 138, no. 1, 2016.

[5] S. Nisar, T. Endo, and F. Matsuno, "Design and kinematic optimization of a two degrees-of-freedom planar remote center of motion mechanism for minimally invasive surgery manipulators," *Journal of Mechanisms and Robotics-Transactions of the Asme*, vol. 9, no. 3, 2017.

[6] D. Stoianovici, L. L. Whitcomb, J. H. Anderson, R. H. Taylor, and L. R. Kavoussi, "A modular surgical robotic system for image guided percutaneous procedures," *Medical Image Computing and Computer-Assisted Intervention - Miccai'98*, vol. 1496, pp. 404–410, 1998.

[7] D. Stoianovici, L. L. Whitcomb, D. Mazilu, R. H. Taylor, and L. R. Kavoussi, "Remote center of motion robotic system and method," U.S. Patent 7,021,173 B2, 2006.

[8] L. Huang, L. Yin, B. Liu, and Y. Yang, "Design and error evaluation of planar 2dof remote center of motion mechanisms with cable transmissions," *Journal of Mechanical Design*, vol. 143, no. 1, p. 013301, 07 2020. [Online]. Available: https://doi.org/10.1115/1.4047519

[9] B. Hannaford, J. Rosen, D. W. Friedman, H. King, P. Roan, L. Cheng, D. Glozman, J. Ma, S. N. Kosari, and L. White, "Raven-ii: An open platform for surgical robotics research," *Ieee Transactions on Biomedical Engineering*, vol. 60, no. 4, pp. 954–959, 2013.

[10] S. Shim, S. Lee, D. Ji, H. Choi, and J. Hong, "Trigonometric ratio-based remote center of motion mechanism for bone drilling," *2018 Ieee/Rsj International Conference on Intelligent Robots and Systems (Iros)*, pp. 4958–4963, 2018.

[11] S. Shim, D. Ji, S. Lee, H. Choi, and J. Hong, "Compact bone surgery robot with a high-resolution and high-rigidity remote center of motion mechanism," *Ieee Transactions on Biomedical Engineering*, vol. 67, no. 9, pp. 2497–2506, 2020.

[12] T. R. Solomon and T. G. Cooper, "Multi-ply strap drive trains for surgical robotic arms," U.S. Patent 9.261,172 B2, 2016.

[13] A. Gijbels, N. Wouters, P. Stalmans, H. Van Brussel, D. Reynaerts, and E. Vander Poorten, "Design and realisation of a novel robotic manipulator for retinal surgery," *2013 Ieee/Rsj International Conference on Intelligent Robots and Systems (Iros)*, pp. 3598–3603, 2013.

[14] D. Stoianovici, K. Cleary, A. Patriciu, D. Mazilu, A. Stanimir, N. Craciunoiu, V. Watson, and L. Kavoussi, "Acubot: A robot for radiological interventions," *Ieee Transactions on Robotics and Automation*, vol. 19, no. 5, pp. 927–930, 2003.

[15] D. Stoianovici, C. H. Jun, S. Lim, P. Li, D. Petrisor, S. Fricke, K. Sharma, and K. Cleary, "Multi-imager compatible, mr safe, remote center of motion needle-guide robot," *Ieee Transactions on Biomedical Engineering*, vol. 65, no. 1, pp. 165–177, 2018.

[16] S.-M. Park, J. Park, H. S. Jang, Y. W. Heo, H. Han, H.-J. Kim, B.-S. Chang, C.-K. Lee, and J. S. Yeom, "Biportal endoscopic versus microscopic lumbar decompressive laminectomy in patients with spinal stenosis: a randomized controlled trial," *The Spine Journal*, vol. 20, no. 2, pp. 156–165, 2020.

[17] M. D'Souza, J. Gendreau, A. Feng, L. H. Kim, A. L. Ho, and A. Veeravagu, "Robotic-assisted spine surgery: history, efficacy, cost, and future trends," *Robotic Surgery: Research and Reviews*, pp. 9–23, 2019.

[18] Medtronic, "Mazor™ robotic guidance platform," https://www.medtronic.com/en-us/healthcare-professionals/products/surgical-robotics/robotic-systems/mazor-robotic-guidance-system.html, 2025, accessed: 2025-07-31.

[19] Globus Medical, "Excelsiusgps™," https://www.globusmedical.com/musculoskeletal-solutions/excelsiustechnology/excelsiusgps/, 2025, accessed: 2025-07-31.

[20] D. A. E. D. D. W. W. C. Lee, John Y. K.; Bhowmick, "Minimally invasive, robot-assisted, anterior lumbar interbody fusion: A technical note," *J Neurol Surg A Cent Eur Neurosurg*, vol. 74, no. 04, pp. 258–261, Jun 2013. [Online]. Available: http://www.thieme-connect.de/products/ejournals/abstract/10.1055/s-0032-1330121

[21] M. Bozkurt, N. Apaydin, Isik, Y. G. Bilgetekin, H. I. Acar, and A. Elhan, "Robotic arthroscopic surgery: a new challenge in arthroscopic surgery part-i: Robotic shoulder arthroscopy; a cadaveric feasibility study," *International Journal of Medical Robotics and Computer Assisted Surgery*, vol. 7, no. 4, pp. 496–500, 2011.

[22] ConvergenceMedical, "V01 surgical robot, the world's first arthroscopic robot." https://www.convergenceortho.com/, 2025, accessed: 2025-07-31.

[23] K. N. Kunze, D. Ferguson, A. Pareek, and N. Colyvas, "Robotic-assisted arthroscopy promises enhanced procedural efficiency, visualization, and control but must overcome barriers to adoption," *HSS Journal®*, p. 15563316251340983, 2025.

[24] J. M. Li, G. K. Zhang, Y. Xing, H. B. Liu, and S. X. Wang, "A class of 2-degree-of-freedom planar remote center-of-motion mechanisms based on virtual parallelograms," *Journal of Mechanisms and Robotics-Transactions of the Asme*, vol. 6, no. 3, 2014.

[25] Z. Yaniv, "Which pivot calibration?" *Progress in Biomedical Optics and Imaging - Proceedings of SPIE*, vol. 9415, 03 2015.

[26] N. P. Dillon, L. B. Kratchman, M. S. Dietrich, R. F. Labadie, R. J. I. Webster, and T. J. Withrow, "An experimental evaluation of the force requirements for robotic mastoidectomy," *Otology Neurotology*, vol. 34, no. 7, pp. e93–e102, 2013.

[27] J. R. Kusins, O. R. Tutunea-Fatan, G. S. Athwal, and L. M. Ferreira, "Analysis of the process parameters affecting the bone burring process: An in-vitro porcine study," *The International Journal of Medical Robotics and Computer Assisted Surgery*, vol. 15, no. 5, p. e2028, 2019.